

Enhancements of Long Term Ionospheric Anomaly Monitoring for the Ground-Based Augmentation System

Jiyun Lee*

Tetra Tech AMT

Sungwook Jung

*Korea Advanced Institute of Science and Technology**

and

Sam Pullen

Stanford University

ABSTRACT

Extremely large ionospheric gradients can pose a potential integrity threat to the users of ground-based augmentation systems (GBAS). A better understanding of the ionospheric behavior (not limited to that during extreme ionospheric activity) is important in the design and operation of GBAS to meet its integrity and availability requirements. A tool for long-term ionosphere monitoring was developed to build an ionosphere threat model, evaluate its validity over the system operation, monitor ionospheric behavior continuously, and update it when necessary. This paper presents the enhanced algorithms of long-term ionospheric anomaly monitoring and evaluates its performance using data from a ionospheric storm day, 20 November 2003, and a nominal day, 9 November 2004. The automation of data processing enables us to more accurately categorize ionospheric behavior under both nominal and anomalous conditions. This paper also demonstrates that the automated procedure of enhanced long-term ionosphere monitoring not only identifies gradients large enough to threaten GBAS users but periodically generates reliable statistics of ionospheric gradients under all conditions.

1.0 INTRODUCTION

Ground-Based Augmentation Systems (GBAS), such as the U.S. Local Area Augmentation System (LAAS), support aircraft precision approach and landing by providing differential corrections and integrity information to aviation users. GBAS reference stations monitor any failures or threats which may pose potential integrity risk to the system. One of the most challenging hazards to mitigate is extreme ionospheric spatial gradients that may occur during severe ionospheric storms. Ionospheric gradients of as large as 413 mm/km

have been observed in the United States during ionospheric storms since April 2000 [1]. The discovery of gradients of this magnitude was a major surprise to the GBAS and LAAS community. The residual range error suffered by a LAAS user at the 200-foot decision height (DH) for a CAT I approach could be as large as 8 meters if such gradients were not observed by the LAAS ground facility (LGF). The configuration of the LGF, user aircraft, ionosphere front, and affected GPS satellite is illustrated in Figure 1. Thus, it required the development of the ionospheric threat model for LAAS use in the Conterminous U.S. (CONUS) to simulate worst-case ionospheric errors that LAAS users might suffer and to develop mitigation strategies [2], [3].

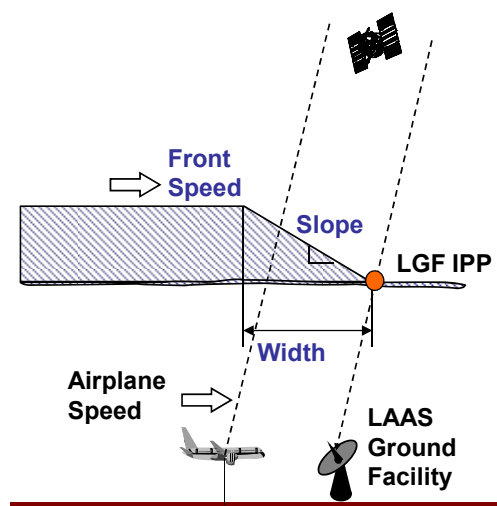


Figure 1: Illustration of a LAAS user impacted by an ionospheric wave-front (modeled as a linear semi-infinite wedge with the slope of the ramp, its width, and constant propagation speed)

The current ionospheric threat model for LAAS, a GBAS developed by the U.S. Federal Aviation Administration (FAA), in CONUS [1] was derived by processing data collected from networks of Continuously Operating Reference Stations (CORS) and Wide Area Augmentation System (WAAS) reference stations. The ionospheric front is modeled as a spatially linear semi-infinite wedge (parameterized by the slope of the ramp and its width) moving with a constant speed as shown in Figure 1. However, the threat model has limitations because it is based upon on a small number of severe ionospheric events whose probability cannot be determined due to the lack of sufficient data. In addition, the receiver separations within the CORS network (typically 40 – 100 km) do not reflect the GBAS architecture, given that the distance between the LGF and users at the CAT I decision height (DH) is no more than 5 – 10 km. Thus, it is not acceptable to rely upon the existing threat model indefinitely.

An automated procedure for long-term ionosphere monitoring is needed to continually monitor ionosphere behavior over the operation period of GBAS as long as GBAS is dependent on the outer bounds of ionospheric threat models. The procedure automatically processes data collected from external sources and networks and estimates ionospheric gradients at regular intervals. If extremely large gradients hazardous to GBAS users are identified, manual validation is triggered. We developed a methodology of long-term ionospheric anomaly monitoring and demonstrated that it successfully identifies the extremely large gradients which can potentially challenge the current threat model [4].

Another important role of long term ionospheric anomaly monitoring is to supply broader statistical information of nominal and anomalous ionospheric behavior in addition to observe and quantify extreme ionospheric events. The realization of this objective requires the enhancement of the long term ionosphere monitoring with an emphasis on the precise estimation of ionospheric delay measurements and automation of procedures. Section 2 introduces the dual-frequency GPS data used in this work. In Section 3, an enhanced methodology for long-term ionospheric anomaly monitoring is presented with an emphasis on key techniques to improve the “simple Truth” processing and automated screening. Monitoring results from case studies are presented in Section 4. Section 5 reviews a method to compute vertical ionospheric gradients and discuss statistical results from case studies. This study is concluded in Section 6.

2.0 DATA

High-quality ionospheric measurements are essential for the long-term ionospheric anomaly monitoring. Precise estimates of ionospheric delays can be obtained using

dual-frequency GPS data from networks of stations and sophisticated post-processing algorithms. The current ionospheric threat model for LAAS was built using ionospheric delay estimates produced by the Jet Propulsion Laboratory (JPL). They collected data from the CORS and WAAS network stations and post-processed those in the “Supertruth” processing described by Komjathy [5]. The JPL solution is very accurate, but because of time-consuming algorithms it is not adequate for being used in near real-time applications. We developed a new method of generating “simple Truth” data, which is simpler and faster than “Supertruth” processing [4]. This method also uses dual-frequency GPS data collected from the CORS network [6] to generate precise ionospheric delay estimates.

The dates from which data were collected and analyzed to evaluate the performance of long term ionospheric anomaly monitoring are shown in Table 1. The conditions on these dates are shown with two indices of global geomagnetic activity from space weather databases: planetary K (K_p) and *disturbance, storm time* (D_{st}), and geomagnetic storm class (G-class), and WAAS coverage. K_p represents solar particle effects on the Earth’s magnetic fields, and is a three-hour composite index measured at several mid-latitude stations primarily located in the northern hemisphere [7, 8]. The K_p index ranges from 0 (no activity) to 9 (extreme activity) in thirds of an index unit. The D_{st} index measures equatorial magnetic disturbance derived from hourly scaling of low-latitude horizontal magnetic variation [9, 10]. A negative D_{st} with the higher magnitude indicates that the more intense magnetic storm is in progress. The storm classes, developed by the Space Weather Prediction Center (SWPC) of the National Oceanic and Atmospheric Administration (NOAA), in order of increasing intensity are: minor, moderate, strong, severe, and extreme.

Table 1: Dates and conditions analyzed for case studies.

Day (UT mm/dd/yy)	K_p	D_{st}	Geomagnetic Storm class	WAAS coverage
11/20/03	8.7	-472	Extreme	~0%
11/09/04	8.7	-223	Severe	~96%

During the well-known 20 November 2003 ionospheric storm, the percentage of WAAS coverage, which indicates the degree to which the storms limited WAAS availability for precision approach, was nearly zero. Within this data set, the maximum gradient in slant ionospheric delay as large as 413 mm/km was observed and verified from the previous study [1]. The geomagnetic storm class on 9 November 2004 was ‘severe’. However, early work demonstrated that the ionospheric activity on this date did not produce any ionospheric spatial gradients greater than 25 mm/km.

Anomalies smaller than this magnitude would not be a significant threat to GBAS users, and thus this date can be classified as a nominal day. Automated procedures of long term monitoring were tested and gradient statistics were obtained using data from these two dates. Those results are shown in Sections 4 and 5 respectively.

3.0 METHODOLOGY

A methodology for long term ionospheric observation and anomaly monitoring was developed based on the data-analysis and verification techniques used to generate the current threat model [4]. This procedure is composed of three steps (as shown in Figure 2): External Data Gathering, Internal Processing, and Manual Validation. The first two steps are completely automated procedures, while the last one is a manual procedure that requires personal intervention. This paper summarizes each step and describes enhancements made to the algorithms presented in [4].

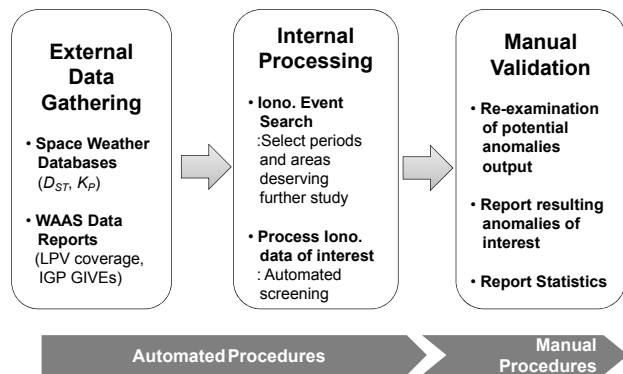


Figure 2: Methodology of long-term ionospheric anomaly monitoring.

3.1 EXTERNAL DATA GATHERING

The automated tool first gathers external information from public space weather sites and the WAAS data reports at regular intervals. This external data is used to select potential periods and areas of anomalous ionospheric events in internal processing. First, the indices of global geomagnetic activity automatically collected from the ftp server of NOAA are: planetary K (Kp) and *disturbance, storm time* (Dst) [11, 12]. To operate this monitoring system on a daily basis (as a default), it requires external data with a data rate of at least once per day. Thus, we use the estimated value of Kp provided by the SWPC of NOAA with an update rate of every three hours 0, and the real-time Dst (known as “Quick-look”) provided every hour by the World Data Center for Geomagnetism at Kyoto University 0.

The WAAS test team of the FAA William J. Hughes Technical Center provides ionospheric vertical delays and Grid Ionospheric Vertical Errors (GIVEs) at geographically fixed Ionospheric Grid Points (IGPs) [14]. This information is updated every three minutes. The WAAS GIVEs, contained in WAAS Message Type (MT) 26, can be used as an indicator of anomalous ionosphere. Especially in this work, the potential areas where ionospheric anomalies may be discovered are selected based on the GIVEs at each grid point.

3.2 INTERNAL PROCESSING

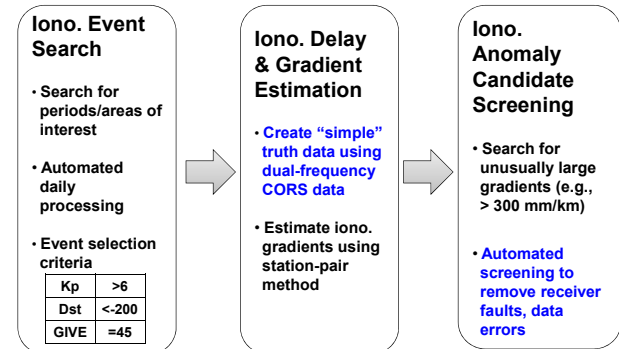


Figure 3: Procedures of internal processing.

The second step is internal processing which consists of Ionosphere Event Search (IES), Ionospheric Delay and Gradient Estimation (IDGE), and Ionospheric Anomaly Candidate Screening (IACS). Figure 3 shows the procedures of internal processing. IES flags periods and areas of interest for further automated analysis if parameters from external sources exceed pre-determined thresholds. IDGE creates “simple Truth” data using dual-frequency CORS data and computes ionospheric gradients using the “simple Truth” data and the station-pair method [4]. IACS automatically searches for any anomalous gradients which exceed a threshold and also pass those to automated false-alarm screening. The selected anomaly candidates will be manually validated at the last step (the details are in Section 3.3). The algorithms of IDGE and IACS with an emphasis on enhancements made (based on the previous version of the tool in [4]) to improve accuracy of ionospheric delay estimates and performance of automation are as follows. Subsection 3.1.A explains the “simple Truth” processing algorithms, and Subsections 3.1.B describes automated screening methods.

3.2.A. Simple Truth Processing

Precise ionospheric delay estimates are generated from the “simple Truth” processing method which is simpler and faster than “Supertruth” processing. Figure 4 shows the procedures of truth processing implemented in this automated tool. The dual-frequency GPS data, automatically collected from the CORS network ftp server, are inputs to the truth processing.

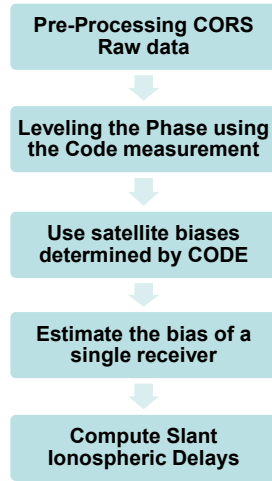


Figure 4: Algorithm for generating “simple Truth” data.

We start from the slant ionospheric delay on the L1 frequency computed from the L1/L2 code and carrier measurements; the code-derived, I_p , and carrier-derived, I_ϕ , observables. The pre-processing of these observables includes cycle slip detection, short arc removal, outlier removal, and code-carrier smoothing as shown in Figure 5. Cycle slip detection is performed for each continuous arc (data gaps between consecutive continuous arcs are greater than 3600 seconds by definition.) Three detection criteria are applied to identify cycle slips of carrier-derived observables. First, a difference between two adjacent data points is examined to detect a large jump greater than 10 meters for a storm day and 0.8 meters for a nominal day. Second, the Loss of Lock Indicator (LLI) of each observation from raw GPS data in RINEX format is utilized as an indicator of potential cycle slips. Third, the absence of both code and carrier measurements is considered as a slip.

Next, we discard data arcs which contain less than ten data points or five minutes in duration because the leveling error of very short arcs is typically large and thus make delay estimates useless. Continuous arcs are divided into several sub-arcs after cycle slip detection and short arc removal. The polynomial fit method is utilized to merge adjacent sub-arcs into one continuous arc. A polynomial fit is performed on sub-arcs. If the differential residuals between sub-arcs are less than 0.8 meters, those are considered as a continuous arc.

After the removal and merging of short arcs, outlier detection and removal are carried out for each continuous arc. Two approaches, the polynomial fit method and the outlier factor method, are executed in parallel. First, a polynomial fit is performed on the carrier-derived observables, I_ϕ , and the differential residuals of the fit are computed. If the largest jump between adjacent points

exceeds an outlier (or slip) detection parameter of 0.8 meters, the jump is classified as a potential outlier.

$$OF(t_p) = \sum_{q \in \text{Adjacent}} w_{pq} \cdot |I_p - I_q|$$

$$w_{pq} = \frac{1/|t_p - t_q|}{\sum_{r \in \text{Adjacent}} 1/|t_p - t_r|} \quad (1)$$

Second, the difference of I between adjacent points is computed using the outlier factor algorithm in [15]. The averaged difference (i.e., Outlier Factor (OF)), between adjacent points of point p at time t_p is calculated by Equation (2). The set “Adjacent” includes all points within five minutes centered at the point p . w is the weight between two points, p and q . If the outlier candidate from the polynomial fit method returns the largest OF , the point is considered as an outlier. We repeat this process until no more outliers remain.

As for the last step of pre-processing, we apply a 150-seconds carrier-smoothing window to smooth the 30-second code-derived observables, I_p , in order to mitigate multipath errors on the code measurements. The outliers of I_p were detected and removed using the polynomial fit method only with a detection threshold of 10 meters.

The carrier-derived observable, I_ϕ , contains integer ambiguities from both L1 and L2 frequencies. To remove these ambiguities, I_ϕ is fitted to I_p , introducing a level parameter, L [4, 5, 16].

$$L = \frac{\sum_{i=1}^N (I_p(t_i) - I_\phi(t_i)) \sin^2 el_i}{\sum_{i=1}^N \sin^2 el_i} \quad (2)$$

The level is computed for each continuous arc by averaging the difference between I_p and I_ϕ over the epoch t_i using an elevation (el)-dependent weighting. To mitigate the multipath effects further, data with elevation angles less than 10 degrees are discarded. The leveled carrier-derived estimates, $I_{\phi_leveled}$, can be written as

$$I_{\phi_leveled} = I_\phi + L = I + \frac{c}{\gamma - 1} (IFB + \tau_{gd})$$

$$\gamma = \frac{f_{L1}^2}{f_{L2}^2} \quad (3)$$

In Equation (3), the receiver and satellite hardware biases (IFB and τ_{gd}) must be removed to obtain ionospheric delay estimates, I . The parameter γ is the squared L1/L2 frequency ratio and c is the speed of light in a vacuum.

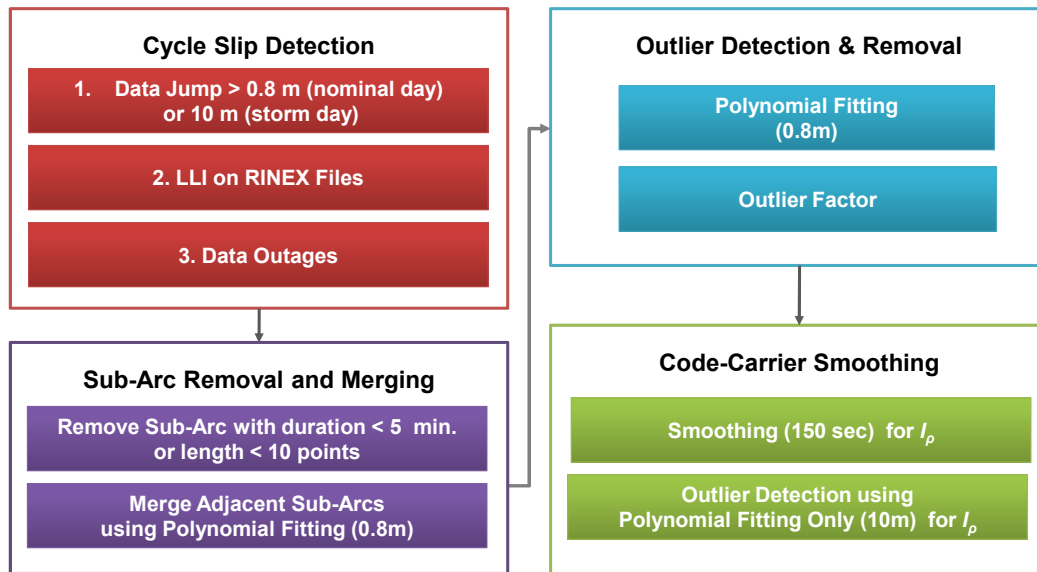


Figure 5: Pre-Processing Procedures.

The next step is to calibrate inter-frequency biases. We follow Ma and Maruyama [16], in which a simpler and faster method to estimate a single receiver IFB is proposed under the condition that satellite biases are known. We use the satellite biases provided by the International GNSS Service (IGS). The IGS product can be obtained from four Global Data Centers (GDCs) [17, 18]. The underlying assumption of this method is that the variation of vertical ionospheric delays from all visible satellites at a given instant becomes minimal when the IFBs are correctly removed. The leveled carrier-derived estimates, $I_{\phi, leveled}$, from Eq. (3) are converted to equivalent vertical delays via a geometric mapping function, and used as inputs to a search algorithm. The best estimate of each receiver IFB is determined by searching for the one which minimizes the cumulative standard deviation of vertical ionospheric delays to their mean on a given day. An elevation cut-off angle of 30 degrees was applied for this algorithm to improve estimation accuracy.

After removing both receiver and satellite hardware biases from $I_{\phi, leveled}$, we obtain precise ionospheric delay estimates, i.e., “simple Truth” data. Using this “simple Truth” solution and the well-known station pair method [1], the automated tool computes ionospheric gradients, ∇I , from all possible pairs of selected CORS stations looking at each satellite [4].

3.2.B. Automated False-Alarm Screening Process

An automated process searches for any severe ionospheric gradients, ∇I , which exceeds a threshold (currently 300 mm/km in slant domain). A considerably large amount of these gradients is not due to ionospheric events. Thus, an automated false-alarm screening process is added to

eliminate those caused by any receiver faults or post-processing errors. To improve the performance of false-alarm detection, we implemented two automated screening methods; negative delay check and excessive-bias check. Cases for which ionospheric delay estimates from one receiver have negative values or do not vary over time are attributed to a faulty receiver. These cases often exhibit a large bias on delay estimates resulting in misleading large gradients. First, the negative delay check eliminates candidates which show the negative values of delay estimates. During extreme ionospheric activities, erratic variations of gradients in time are typically observed. Thus, ionospheric gradients which are extremely large but steady over time are most likely false candidates. The excessive-bias check computes the mean of ionospheric gradients of a sub-arc where an anomaly candidate is identified. If all of the differences between gradients and the mean are less than 50 km/mm, the candidate is discarded in this process. The new methods effectively discriminate misleading ionospheric anomaly candidates, which will be shown in Section 4.0.

3.3 MANUAL VALIDATION

Once the automated tool has isolated an apparently anomalous set of data, manual inspection is required to validate that the observed events are actually due to the ionosphere and not CORS receiver faults or data errors. While approaches to manual validation will vary based on the details of the automated outputs, the typical method is to re-examine the L1/L2 dual-frequency estimates visually to determine whether the resulting gradients look “reasonably” like ionospheric events. Dual-frequency data are prone to L2 (semi-codeless) loss of lock, particularly for satellites at low elevation angles. We compare the

dual-frequency estimates with the estimates based on only the L1 frequency code-carrier divergence. This L1-only measurement is more robust to outages and cycle slips. If both the dual-frequency and single-frequency estimates are in agreement, the gradient is declared to be “validated.”

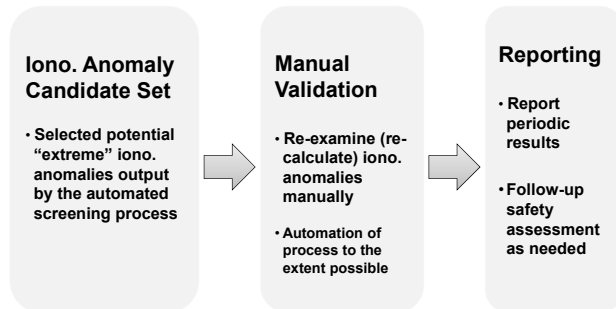


Figure 6: Procedures of Manual validation and Reporting.

If an anomalous event is substantially validated by manual analysis, it will be reported periodically along with gradient statistics. Examples of statistics are shown in Section 5.0. It is expected that commonly nothing requiring manual validation is found in a given time period. In that case, ionospheric statistics from automated procedures will be supplied in periodic reports. The reports will occasionally be filled with manual validation results in addition to automated results statistics. These results would be reviewed and, if they exceed the bounds of the current threat model, a change to that model would be considered.

4.0 MONITORING RESULTS

To examine the performance of the enhanced algorithms of long term ionospheric anomaly monitoring, two case studies were conducted on both nominal (9 November 2004) and ionospheric storm (20 November 2003) days. The results are summarized in Table 2, and details are as follows.

4.1 CASE STUDY I: IONOSPHERIC STORM DAY

On 20 November 2003, both of the space weather indices, Kp of 8.7 and Dst of -472 (see Table 1), exceed the selection criteria of 6 and -200 respectively. This date is thus automatically selected at the step of ionospheric event search (IES). The daily maximum GIVEs at almost all IGP in CONUS are 45 meters, and thus IES conservatively selects the entire CONUS as the area of interest. As of November 2003, the total number of CORS stations in CONUS was 368. The automated tool searches for stations which have nearby stations within 100 km, and the number of such stations is 239. The GPS dual-

frequency data of these stations are automatically downloaded from the CORS ftp server and processed to obtain ionospheric delay and gradient estimates for all possible pairs of stations considering all satellite in view.

Next, Ionospheric Anomaly Candidate Screening (IACS) searched for any anomalous gradients greater than 300 mm/km and returned 45 candidates. Among those, 16 candidates, possibly caused by receiver artifacts or post-processing errors, were removed by the automated false-alarm screening. The automated screening is not faultless either. Thus, we performed manual validation on the remaining 29 candidates, and twelve candidates were finally verified as true ionospheric anomalies.

The twelve anomalies observed from this test are listed in Table 3 with gradient magnitude, baseline length, time of observation, satellite and station pairs. The first ten anomalies are newly observed gradients, whereas the last two anomalies are the worst gradients at low and high elevation discovered from the prior work [1, 4]. Note that, for the case of the worst gradient at high elevation (No. 12 in Table 3), the magnitude of the slope previously estimated using the JPL post-processed CORS truth data was 413 mm/km [1]. Thus, the difference of approximately 26 mm/km exists between the “simple Truth” and CORS truth estimates. However, this discrepancy is acceptable because the estimates are accurate enough to identify the most extreme ionospheric anomalies.

Figure 7 shows the dual-frequency ionospheric gradients (blue) observed from SIDN and KNTN viewing SVN 44 as a function of time. The gradients are calculated by dividing the difference of the “simple Truth” delay estimates by the station separation distance of 59.1 km. Data outages on dual-frequency estimates are visible in this plot, calling into question the reliability of the maximum slope of 367 mm/km at about 41.4 deg elevation and 2107 UT. For this reason, the manual validation was conducted by comparing the dual-frequency estimates (blue) with the L1 code-minus-carrier estimates of the slope (red). The data outages do not exist in the single-frequency estimates which are not subject to fragile L2 semicodeless tracking loops. Based on the good agreement of the two slope estimates, this event was verified as a real ionospheric anomaly (No. 9 in Table 3). All other anomalies in Table 3 were also validated through this manual validation procedure. For the cases of No. 5 and 6, dual-frequency estimates and single frequency estimates exhibited very similar patterns of ionospheric gradient. However, two estimates showed considerable differences in magnitude. The final gradient estimates, 268 mm/km and 243 mm/km, were determined based on the L1-only estimates which form a lower bound on the true gradient, and thus those are less than the monitoring threshold of 300 mm/km.

Table 2: Summary of long-term ionospheric anomaly monitoring results from two case studies.

–		20 Nov. 2003	09 Nov. 2004
Total Number of CORS Receivers in CONUS		368	506
Number of Stations with Baseline ≤ 100 km		239	331
Initial Ionospheric Anomaly Candidate Screening (Ionospheric Gradients > 300 mm/km, Satellite – Station Pair)		45	23
Automated Screening	Removed from Negative Delay Check	2	11
	Removed from Excessive Bias Check	14	12
Final Ionospheric Anomaly Candidates (Satellite – Station Pair)		29	0
Manually Validated Ionospheric Anomalies (Satellite – Station Pair)		12	0

Table 3: Summary of manually validated ionospheric anomalies observed on 20 November 2003 in CONUS.

No.	Station	Latitude (degree)	Longitude (degree)	Baseline (km)	SVN	Time (UT)	Gradient (mm/km)	Elevation (degree)
1	GRTN	38.9	-83.9	76.9	44	21:07:00	305.4	56.4
	PKTN	39.0	-83.0					
2	ERLA	39.0	-84.6	65.6	44	21:09:30	315.3	57.4
	GRTN	38.9	-83.9					
3	GODE	39.0	-76.8	23.7	38	20:56:00	304.3	67.5
	USNO	38.9	-77.1					
4	PKTN	39.0	-83.0	85.2	44	21:04:00	313.7	54.5
	STKR	39.3	-82.1					
5	ERLA	39.0	-84.6	53.1	44	21:09:30	268.2	57.8
	LEBA	39.4	-84.3					
6	FREO	40.2	-81.3	77.4	44	20:59:30	243.4	52.8
	MCON	39.7	-81.8					
7	COLB	40.0	-83.0	65.4	44	21:02:00	371.5	54.8
	MTVR	40.4	-82.5					
8	FREO	40.2	-81.3	73.6	26	21:16:00	335.6	10.6
	LSBN	40.8	-80.8					
9	KNTN	40.6	-83.6	59.1	44	21:07:30	367	41.4
	SIDN	40.3	-84.2					
10	MTVR	40.4	-82.5	65.5	44	21:00:30	307.1	54.2
	WOOS	40.8	-82.0					
11	GARF	41.4	-81.6	74.5	26	21:17:00	351.7	11.4
	WOOS	40.8	-82.0					
12	GARF	41.4	-81.6	51.2	38	20:59:30	386.8	68.4
	ZOB1	41.3	-82.2					

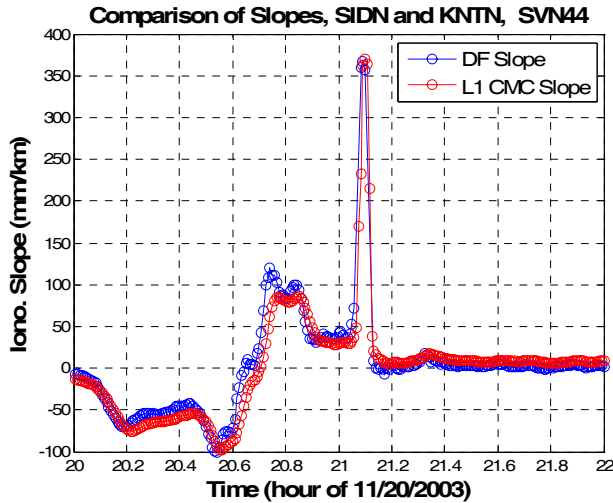


Figure 7: Comparison of dual-frequency (blue) and single-frequency (red) spatial gradient estimates between SIDN and KNTN viewing SVN 44 at mid-elevation, as a function of time.

4.2 CASE STUDY 2: NOMINAL DAY

On 9 November 2004, no gradients greater than 25 mm/km were observed from the previous work [19], and thus this date is classified as a nominal day. The total number of CORS receivers in CONUS as of November 2004 was 506. Among those, the number of stations which have nearby stations within 100 km is 331. Ionospheric gradients were calculated for all possible pairs of 331 CORS stations and all satellite in view. The automated process first searched for any gradients which exceed 300 mm/km for this test, and it returned 23 candidates. Next, the automated false-alarm screening process successfully eliminated all 23 false candidates. The results are summarized in Table 2. From this case study, we conclude that the long term ionospheric anomaly monitor performs as expected also on nominal days (i.e., it did not return any faulty anomaly candidates).

5.0 STATISTICS OF IONOSPHERIC GRADIENTS

The enhanced algorithms of long term ionospheric monitoring provide ionospheric gradient statistics under both nominal and anomalous conditions. So far when we discuss ionospheric anomalies in previous sections, we expressed gradient estimates in the “slant domain”. Statistics of those gradients are often driven in the “vertical domain” because ionospheric delay varies with satellite elevation. Subsection 5.1 revisits a method to compute vertical ionospheric gradients using the station-pair method. Subsections 5.2 and 5.3 present gradient statistics obtained from two case studies on a nominal day (9 November 2004) and an ionospheric storm (20 November 2003) day.

5.1 VERTICAL IONOSPHERIC GRADIENT

Slant ionospheric delays can be converted into equivalent vertical delays using a geometric mapping function derived by approximating the ionosphere with a thin-shell model. The model assumes that the entire ionosphere is condensed at a shell located at 350 km from the ground. The mapping function M or “obliquity factor” is expressed as

$$M(el, h_I) = \left[\cos \left(\sin^{-1} \left(\frac{R_e \cos(el)}{R_e + h_I} \right) \right) \right]^{-1} \quad (4)$$

where R_e is the radius of the Earth, h_I is the height of the thin shell, and el is the elevation angle of the line of sight (LOS) between a receiver and a satellite. By dividing a slant delay, I_{slant} , by the obliquity factor, we can convert it to the equivalent vertical delay, $I_{vertical}$, experienced by a user directly under the ionospheric pierce point (IPP) where a LOS and the thin shell model intersect.

$$I_{vertical} = \frac{I_{slant}}{M(el, h_I)} \quad (5)$$

The station-pair method [19] shown in Figure 8 is used to compute vertical ionospheric gradients, vig . We differentiate vertical ionospheric delays of two stations, S_1 and S_2 , and divide it by the IPP distance, d_{IPP} , as shown in Equations (6) and (7).

$$dI_{vertical} = I_{vertical, S1} - I_{vertical, S2} \quad (6)$$

$$vig = \frac{dI_{vertical}}{d_{IPP}} \quad (7)$$

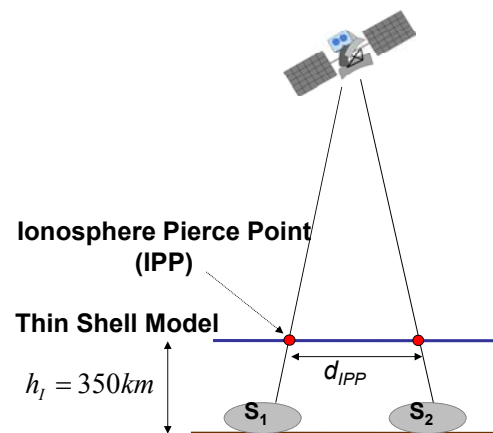


Figure 8: Station pair method.

5.2 STATISTICS RESULTS ON NOMINAL DAY

Excess noise and bias errors in the “simple Truth” data need to be removed to the extent possible to obtain reliable statistics of ionospheric spatial gradients. To exclude noisy measurements (due to multipath and receiver noise), we applied an elevation cutoff angle of 30 degrees. To remove the remaining biases including the leveling error of carrier observables and the IFB calibration error, we leveled differential ionospheric delays by subtracting off the mean of differential ionospheric delays of continuous arcs. The continuous arcs were determined by applying the slip detection parameters of 5-15 cm depending on IPP separation distances.

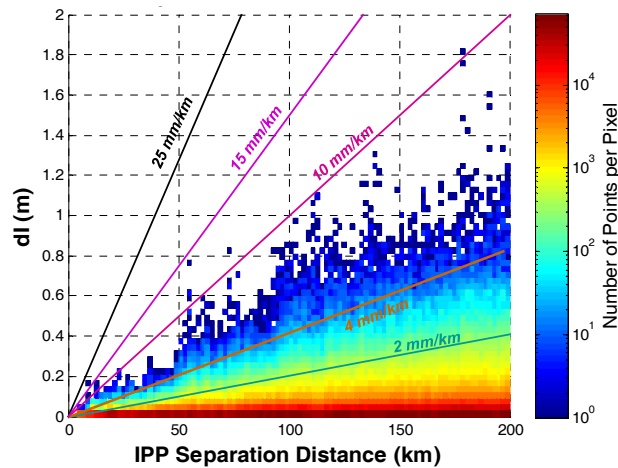


Figure 9: Differential vertical ionospheric delay results on a nominal day (9 November 2004) from “simple Truth” data.

Figure 9 shows the spatial decorrelation result for a nominal day (9 November 2004) using the “simple Truth” data and the station-pair method. The horizontal axis divides the IPP separation distances into bins, and the vertical axis divides observations of the difference in vertical ionospheric delays into bins. The color of each pixel presents the number of measurements counted. The differential delays were divided by the corresponding IPP distances to compute vertical ionospheric gradients. The level of geomagnetic activity on this day was severe, and thus a large number of measurements fall in between 4 and 10 mm/km (note that 4 mm/km is the standard broadcast one-sigma value which was chosen as a conservative bound on nominal vertical ionospheric spatial gradients [19].) However, no gradients greater than 25 mm/km were observed as expected. This supports that the “simple Truth” processing combined with noise reduction and bias removal provides precise and reliable gradient estimates also on nominal days.

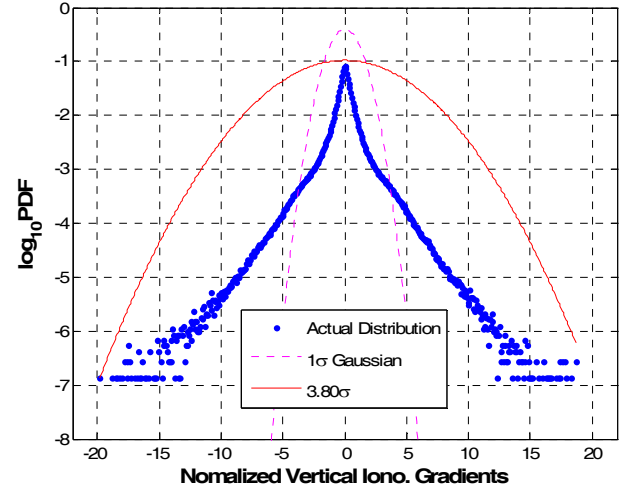


Figure 10: Probability density function of normalized vertical ionospheric gradients on a nominal day (9 November 2004).

The distribution of normalized vertical ionospheric gradients is shown in Figure 10 on a logarithmic scale. The vertical gradients are normalized by removing their mean and dividing them by their standard deviations. It is clearly seen that the distribution (the dotted blue curve) derived from the observations shown in Figure 9 has non-Gaussian tails. Because LAAS users assume a zero-mean normally distributed error model in the computation of protection levels, the nominal sigma (1σ) of a zero-mean Gaussian distribution (shown as the dashed curve) should be inflated to cover the non-Gaussian tails of the actual distribution. The inflation factor (f) needed for the data on 9 November 2004 was 3.80.

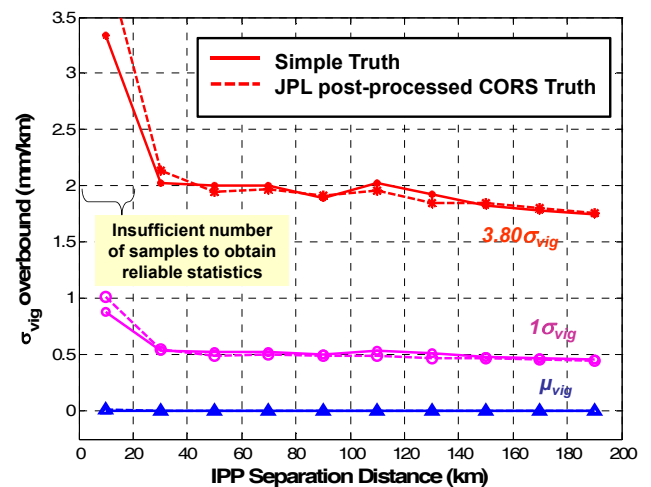


Figure 11: σ_{vig} overbound results from “simple Truth” data and CORS Truth data for a nominal day (9 November 2004).

To determine “ σ_{vig} overbound”, first vertical ionospheric gradients are divided into bins of IPP distance. Second, we compute the mean (μ_{vig}) and standard deviation (σ_{vig}) of vertical ionospheric gradients in each bin, and use those to normalize the gradients. Lastly, the “ σ_{vig} overbound” is computed as $|\mu_{vig}| + f \sigma_{vig}$ for each bin. Figure 11 shows the σ_{vig} overbound result for a nominal day (9 November 2004). The curves with blue triangles, pink circles and red asterisks show the means, the one-sigma values and the σ_{vig} overbounds, respectively. The estimates at the IPP separation less than 20 km cannot be trusted because of insufficient number of samples to obtain reliable statistics. This figure compares statistics derived from two truth data; the “simple Truth” data (solid lines) and the CORS Truth data (dashed lines). The two σ_{vig} overbounds agree well, which indicates that the quality of “simple Truth” data is accurate enough to provide reliable statistical data.

5.3 STATISTICS RESULTS ON IONOSPHERIC STORM DAY

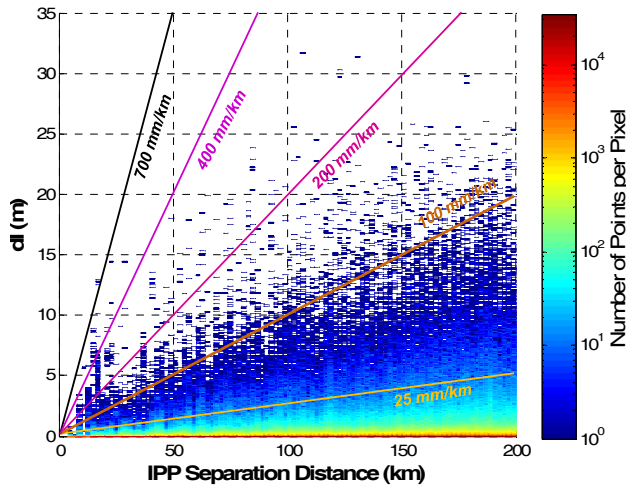


Figure 12: Differential vertical ionospheric delay results on an ionospheric storm day (20 November 2003) before removing faulty anomaly candidates.

Figure 12 shows a two-dimensional histogram of measurements as a function of the IPP separation distance and the differential ionospheric delay in vertical domain for the well-known ionospheric storm day, 20 November 2003. The maximum verified gradient on this date is known as 413 mm/km (in the slant domain) from the prior work. However, this plot shows several observations between 400 and 700 mm/km. That is because the figure includes faulty ionospheric anomaly candidates which should be eliminated by the automated screening process or manual validation. After removing faulty anomaly candidates, we plotted the histogram again which is shown in Figure 13. It is clearly seen that no gradients larger than 400 mm/km were identified. The pixel within

the red circle contains the worst gradient observed at high elevation. Because the observations in this figure are expressed in the vertical domain, the anomaly in the red circle is slightly less than 400 mm/km.

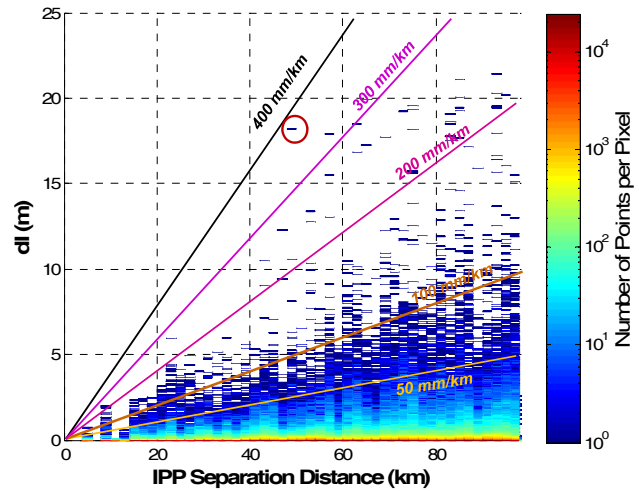


Figure 13: Differential vertical ionospheric delay results on an ionospheric storm day (20 November 2003) after removing faulty anomaly candidates.

The distribution of normalized vertical ionospheric gradients is shown in Figure 14. The actual distribution (the dotted blue curve) is derived from the empirical data shown in Figure 13. The tails of the distribution on this ionospheric storm day are much thicker than those on the nominal day, because severely large gradients exhibit in a wide range. The inflation factor to overbound the actual distribution of vertical gradients is 9.43.

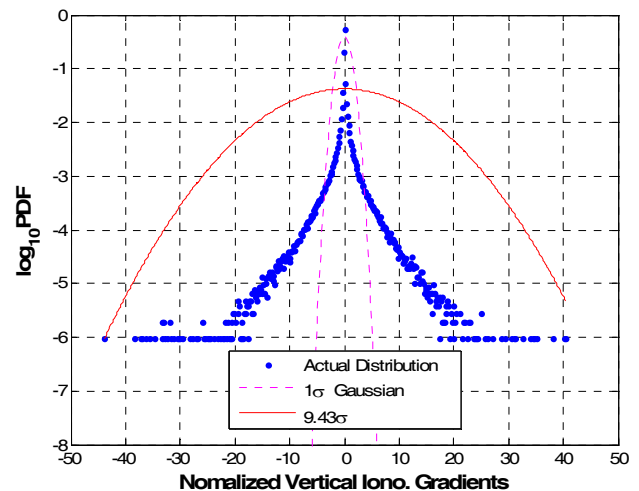


Figure 13: Probability density function of normalized vertical ionospheric gradients on an ionospheric storm day (20 November 2003).

6.0 CONCLUSION

This paper presents an enhanced methodology of long-term ionosphere monitoring to continuously monitor ionospheric events and check the validity of the current threat model over the life cycle of GBAS. The automation of monitoring procedures needs to be improved to limit the number of “false” gradients passed on to manual validation and to supply broader statistical estimates of nominal and anomalous ionospheric behavior. Especially improved truth data is needed to provide gradient statistics. We matured the tool by improving accuracy of ionospheric delay estimates and performance of automation.

The results from case studies support that the use of “simple Truth” data should be sufficient to identify extreme ionospheric anomalies which may challenge the current threat model. The improved “simple Truth” data is also shown to produce reliable gradient statistics. Once the tool is in permanent operation, it will help to understand statistics surrounding a severe event, to estimate the occurrence of such event, and to more accurately categorize nominal and anomalous ionospheric conditions. This will consequently improve the GBAS design with enhanced integrity and availability. This knowledge should also benefit future GBAS operations, including those separate from the “straight-in” CAT I approaches that are now supported.

ACKNOWLEDGMENTS

The authors thank the Federal Aviation Administration (FAA) Local Area Augmentation System (LAAS) Program Office, of whom Carlos Rodriguez and Jason Burns were particularly helpful. We also would like to thank Tom McHugh of the FAA William J. Hughes Technical Center, Attila Komjathy of the Jet Propulsion Laboratory, Masahito Nose of Kyoto university, and Per Enge, Ming Luo, Godwin Zhang, Seebany Datta-Barua, Todd Walter, and Juan Blanch of Stanford for their support of this work.

REFERENCES

1. Datta-Barua, S., Lee, J., Pullen, S., Luo, M., Ene, A., Qiu, D., Zhang G., and Enge, P., “Ionospheric Threat Parameterization for Local Area GPS-Based Aircraft Landing Systems,” *AIAA Journal of Aircraft*, Vol. 47, No. 4, Jul. 2010, pp. 1141-1151.
2. Lee, J., Luo, M., Pullen, S., Park, Y. S., Enge, P., and Brenner, M., “Position-Domain Geometry Screening to Maximize LAAS Availability in the Presence of Ionosphere Anomalies,” *Proceedings of ION GNSS 2006*, Fort Worth, TX, Sept. 26-29, 2006, pp. 393 - 408.
3. Ramakrishnan, S., Lee, J., Pullen, S., and Enge, P., “Targeted Ephemeris Decorrelation Parameter Inflation for Improved LAAS Availability during Severe Ionosphere Anomalies,” *Proceedings of the 2008 ION National Technical Meeting*, San Diego, CA, Jan. 28-30, 2008, pp. 354 - 366.
4. Lee, J., Jung, S., Bang, E., Pullen, S., and Enge, P., “Long Term Monitoring of Ionospheric Anomalies to Support the Local Area Augmentation System,” *Proceedings of ION GNSS 2010*, Portland, OR, Sept. 21-24, 2010, pp. 2651-2660.
5. Komjathy, A., L. Sparks, and A.J. Mannucci, “A New Algorithm for Generating High Precision Ionospheric Ground-Truth Measurements for FAA's Wide Area Augmentation System,” Jet Propulsion Laboratory, JPL Supertruth Document, Vol. 1, Pasadena, LA, July 2004.
6. National Geodetic Survey (NGS) CORS Team, “CORS: Continuously Operating Reference Stations,” <http://www.ngs.noaa.gov/CORS/> [retrieved 12 Aug. 2010].
7. Menvielle, M., and Berthelier, A., “The K-Derived Planetary Indices: Description and Availability,” *Reviews of Geophysics*, Vol. 29, No. 3, 1991, pp. 415-432.
8. Menvielle, M., and Berthelier, A., Correction to “The K-Derived Planetary Indices: Description and Availability,” *Reviews of Geophysics*, Vol. 30, No. 1, 1992, p. 91.
9. National Geophysical Data Center, “Space Physics Interactive Data Resource,” 2005, <http://spidr.ngdc.noaa.gov/spidr/> [retrieved 1 March 2005].
10. Sugiura, M., and Kamei, T., “Equatorial Dst Index 1957–1986,” *International Association of Geomagnetism and Aeronomy*, Vol. 40, 1991, pp. 7–14.
11. National Geophysical Data Center (NGDC) in National Oceanic and Atmospheric Administration (NOAA), “NOAA/National Geophysical Data Center (NGDC) FTP Service,” <ftp://ftp.ngdc.noaa.gov> [retrieved 25 May 2010].
12. Space Weather Prediction Center (SWPC) in National Oceanic and Atmospheric Administration (NOAA), “Space Weather Prediction Center Anonymous FTP Service,” <ftp://ftp.swpc.noaa.gov> [retrieved 25 May 2010].
13. Kyoto University, “World Data Center for Geomagnetism, Kyoto,” <http://wdc.kugi.kyoto-u.ac.jp> [retrieved 28 May 2010].

14. FAA/William J Hughes Technical Center, "NSTB/Wide-Area Augmentation System Test Team" <http://www.nstb.tc.faa.gov> [retrieved 5 April. 2010].
15. Kou, Y., Lu, C.-T., and Chen, D., "Spatial Weighted Outlier Detection," *Proceedings of the 2006 SIAM International Conference on Data Mining*, Bethesda, MD, Apr. 20-22, 2006, pp. 614-618.
16. Ma, G. and Maruyama, T., "Derivation of TEC and Estimation of Instrumental Biases from GEONET in Japan", *Annales Geophysicae*, Vol. 21, 2003, pp. 2083-2093.
17. Hernández-Pajares, M., Juan, J. M., Sanz, J., Orus, R., Garcia-Rigo, A., Feltens, J., Komjathy, A., Schaer, S. C., and Krankowski, A., "The IGS VTEC Maps: A Reliable Source of Ionospheric Information Since 1988," *Journal of Geodesy*, Vol. 83, No. 3-4, 2009, pp. 263-275.
18. International GNSS Service (IGS) Central Bureau, "International GNSS Service," <http://igscb.jpl.nasa.gov> [retrieved 29 Jan. 2011].
19. Lee, J., Pullen, S., Datta-Barua, S., Enge, P., "Assessment of Ionosphere Spatial Decorrelation for Global Positioning System-Based Aircraft Landing Systems." *AIAA Journal of Aircraft*, Vol. 44, No. 5, Sept. 2007, pp 1662-1669.